Effects of Thermal Aging on Material Properties, Stress Corrosion Cracking, and Fracture Toughness of AISI 316L Weld Metal

Citation: Lucas, Timothy, Antti Forsström, Tapio Saukkonen, Ronald Ballinger, and Hannu Hänninen. "Effects of Thermal Aging on Material Properties, Stress Corrosion Cracking, and Fracture Toughness of AISI 316L Weld Metal." Metallurgical and Materials Transactions A 47, no. 8 (June 14, 2016): 3956–3970.

As Published: http://dx.doi.org/10.1007/s11661-016-3584-6

Publisher: Springer US

Persistent URL: http://hdl.handle.net/1721.1/103861

Version: Author's final manuscript: final author's manuscript post peer review, without publisher's formatting or copy editing

Manuscript submitted on November 26, 2015

Effects of Thermal Aging on Material Properties, Stress Corrosion Cracking, and Fracture Toughness of AISI 316L Weld Metal

T. Lucas[1], A. Forsström[2], T. Saukkonen[2], R. Ballinger[1], H. Hänninen[2]

[1]MIT, 185 Albany Street, Cambridge, MA 02139
[2]Aalto University, PO Box 14200, Espoo, Finland

Corresponding author:

Antti Forsström
antti.forsstrom@aalto.fi
+358 40 531 0905

Aalto University School of Engineering
Department of Mechanical Engineering
Engineering Materials
P.O. Box 14200
FI-00076 Aalto
Finland

Keywords: thermal aging, stainless steel, weld metal, stress corrosion cracking, fracture toughness, impact toughness, spinodal decomposition, G-phase

Abstract

Thermal aging and consequent embrittlement of materials are ongoing issues in cast stainless steels, as well as duplex, and high-Cr ferritic stainless steels. Spinodal decomposition is largely responsible for the well-known "748 K (475 °C) embrittlement" that results in drastic reductions in ductility and toughness in these materials. This process is also operative in welds of either cast or wrought stainless steels where δ-ferrite is present. While the embrittlement can occur after several hundred hours of aging at 748 K (475 °C), the process is also operative at lower temperatures, at the 561 K (288°C) operating temperature of a boiling water reactor (BWR), for example, where ductility reductions have been observed after several tens of thousands of hours of exposure.

An experimental program was carried out in order to understand how spinodal decomposition may affect material properties changes in Type 316L BWR piping weld metals. The study included material characterization, nanoindentation hardness, double loop electrochemical potentiokinetic reactivation (DL-EPR), Charpy-V, tensile, SCC crack growth, and *in-situ* fracture toughness testing as a function of δ-ferrite content, aging time, and temperature.

SCC crack growth rates of Type 316L stainless steel weld metal under simulated BWR conditions showed an approximate 2x increase in crack growth rate over that of the unaged as-welded material. *In-situ* fracture toughness measurements indicate that environmental exposure can result in a reduction of toughness by up to 40% over the corresponding at-temperature air tested values. Material characterization results suggest that spinodal decomposition is responsible for the degradation of material properties measured in air, and that degradation of the *in-situ* properties may be a result of hydrogen absorbed during exposure to the high-temperature water environment.

1. Introduction

Thermal aging and consequent embrittlement are ongoing issues in cast stainless steels [1-4], as well as duplex [5-9], and high-Cr ferritic stainless steels [10, 11]. Spinodal decomposition is largely responsible for the well-known "748 K (475 °C) embrittlement" that results in drastic reductions in ductility and toughness in these materials. This process is also operative in welds of either cast or wrought stainless steels where δ-ferrite is present [12-15]. While embrittlement can occur after several hundred hours of aging at 748 K (475 °C), the process is also operative at lower temperatures, at the 561 K (288°C) operating temperature of a boiling water reactor (BWR), for example, where ductility reductions have been observed after several thousands of hours of exposure [16].

In order to produce a high-quality and functional Type 316 stainless steel weld using automated gas tungsten arc welding (GTAW) it is necessary to control the filler metal wire chemistry to promote the formation of an appropriate amount of δ-ferrite (>5%). The purpose of the δ-ferrite phase dispersed within an austenitic weld metal matrix is to prevent hot cracking during weld solidification. However, at the operating temperatures and time scales concerning nuclear power plant components, δ-ferrite becomes susceptible to spinodal decomposition [16]. When δ-ferrite undergoes spinodal decomposition the structure maintains its body-centered cubic structure, while the δ-ferrite phase separates into a periodically spaced chromium-rich, iron-depleted α'-phase (alpha prime phase), and an iron-rich, chromium-depleted α-phase with a wavelength/separation of approximately 5-10 nm. For more information on the kinetics of spinodal decomposition, see [17]. Additional microstructural changes occurring in the same temperature range are NiSiMo-rich G-phase precipitation ($Ni_{16}Si_7Ti_6$, but substitution of Ti by Cr/Mn, and Ni by Fe/Mo), $M_{23}C_6$ precipitation at δ-ferrite-austenite phase boundaries (with subsequent sensitization), as well as segregation of impurities. Mo-bearing steel containing more Ni are more prone to G-phase precipitation. G-phase formation is a consequence of α' formation and its kinetics is related to the spinodal decomposition kinetics. Spherical G-phase particles form at the α'-α-interfaces due to rejection fluxes of supersaturated Ni from α' and Si from α [6]. G-phase precipitation on dislocations is also observed. G-phase precipitates on the dislocations are larger than those in the matrix [9].

Experiments on aging under tensile loading have shown that the aging kinetics is markedly enhanced and decomposition and clustering become faster the higher the stress [18]. It has been shown that these microstructural changes can lead to significant changes in material properties. Increase in hardness and strength and a decrease in ductility are commonly observed. However, there has been very little research concerning stress corrosion cracking (SCC) of stainless steel welds of this type and little effort to quantify and explain the influence of the microstructural changes that occur during aging on SCC crack growth in high-temperature water environment.

An experimental program was carried out in order to understand how spinodal decomposition may affect the material properties of Type 316L stainless steel BWR piping weld metals. This type of material is used in Japanese BWRs, as well as in the new EPR PWRs [20]. The study included material characterization, nanoindentation hardness, DL-EPR, Charpy-V, tensile, SCC crack growth, and *in-situ* fracture toughness testing as a function of aging time and temperature. The primary metallurgical variable in this research was the amount of δ-ferrite present in the weld metal, produced by automated gas tungsten arc welding (GTAW).

2. Experimental Methods

2.1. Weld Preparation and Aging

Welds replicating those found in BWR water recirculating piping were produced with two ferrite numbers and aged in air for different times and at different temperatures in order to compare and quantify the effects of thermal aging on the material properties. Base material for the welding was forged Type 316L stainless steel pipe 600 mm in diameter with 41.27 mm wall thickness and manufactured by Japan Steel Works.

Welding was performed at the EPRI NDE Center in Charlotte, NC, USA by using automated gas tungsten arc welding with two heats of 316L filler metals. Filler metal chemistry was controlled for separate welds to give a high ferrite number of 14 (Cr_{eq} = 21.8, Ni_{eq} = 12.8) and a low ferrite number of 10 (Cr_{eq} = 21.8, Ni_{eq} = 13.5) according to WRC-92 [19]. The chemical compositions of the weld metals are given in Table 1. Each welded pipe was sectioned in the required geometry presented in Figure 1 and the sample blanks were aged according to the aging matrix presented in Table 2. At each time/temperature combination a sufficient number of blanks were produced for the purpose of Charpy V-notch impact, tensile, SCC crack growth, and fracture toughness testing at 298 K (25 °C) and 561 K (288 °C). [20]

2.2. Material Characterization

2.2.1. Nanoindentation

Effect of thermal aging on δ-ferrite hardness of the high ferrite welds (FN 14) was studied by using a CMS Instruments Nano-Hardness Tester installed on an open platform. Prior to testing the samples were sectioned using electro-discharge machining (EDM). Sample preparation was done by conventional mechanical wet grinding, polishing up to ¼ μm diamond paste, and followed by 4 h of vibratory polishing in non-crystallizing colloidal silica to remove any possible deformation on the surface.

The indentation was done using a Berkovich diamond tip indenter. Indentation force was set to 2.5 mN, loading and unloading rate to 15 mN/min, hold time to 20 s, and Poisson's ratio to 0.30. Oliver & Pharr method was used for curve fitting [21]. The indenter movement was not accurate enough to hit any wanted spot on the specimen at micrometer scale. Therefore, matrices of for example 5x5 had to be used to hit the small areas of δ-ferrite. Distance between indentations was set as 5 μm. After testing, the location of indentation markings was visually inspected (Figure 2) by using an optical microscope included in the nano-hardness tester. Only indentations with a clear hit on δ-ferrite (or austenite) were accepted as data points. Indentations were taken from the root, middle, and crown of the welds. At least 10 good hits on δ-ferrite was set as a requirement from each of the aforementioned weld regions. This resulted in a total number of 200 to 400 indentations per weld region, most of which were on austenite.

2.2.2. DL-EPR

Double-loop electrochemical potentiokinetic reactivation tests (DL-EPR) were conducted **according to international standard ISO 12732 [22]** to study the effect of thermal aging on corrosion resistance of

the welds. The same high ferrite welds (FN 14) were used as in the nanoindentation measurements by EDM cutting circular specimens (ø16 mm) from the middle of the welds. The specimens were re-polished to roughness of ¼ μm with diamond pastes, followed by 4 h in a vibratory polisher in non-crystallizing colloidal silica.

The DL-EPR tests were done in stronger than standard 1M H_2SO_4 + 0.1M KSCN solution. This was because no reactivation peak was observed with the standard 0.5M H_2SO_4 + 0.01M KSCN solution for 304 stainless steel [22]. By using the stronger solution it was possible to make the effect of thermal aging visible in the reactivation scan. 500 mL of fresh test solution was used for every run. A saturated calomel electrode (SCE) was used as the reference electrode. Prior to testing the specimens were cathodically polarized to -1 V_{SCE} for 120 s to remove the air-formed oxide film. The specimens were then kept at the free corrosion potential for 2 min, scanned with a scanning rate of 1.67 mV/s from the free corrosion potential to +300 mV_{SCE}, and back to the free corrosion potential with the same scanning rate. After DL-EPR testing the specimens were examined in SEM.

2.2.3. SEM Studies

Scanning electron microscopy (SEM) was performed with a Zeiss Merlin VP Compact Field Emission Gun FEG-SEM equipped with a QUANTAX 800 EDS analyzer and Oxford Instruments Nordlys II EBSD detector. The sample preparation prior to nanoindentation studies was checked with EBSD to ensure minimum plastic deformation on the surface of the specimens.

2.2.4. Stress Corrosion Cracking

Stress corrosion cracking (SCC) tests were conducted in simulated boiling water reactor (BWR) conditions. The BWR environment was controlled using a custom-built water purification and chemistry control system connected to an autoclave. The autoclave and any associated piping that operated at a temperature above 423 K (150 °C) were constructed of titanium. A pressurization, temperature and chemistry control system maintained the sample and surrounding water at 561 K (288 °C) and, with the assistance of a charging pump and back pressure regulator, at 7.5 MPa and a dissolved oxygen concentration of 300 ppb. Loading of the sample was applied and controlled by an Instron® 8800MR load frame and controlled by a custom program receiving input from the data acquisition and control system (DAC). The DAC system measured all relevant parameters of the system including temperature, pressure, load, chemistry as well as providing control for loading and stress intensity factor (K). SCC tests were conducted at constant K. Measurement of crack length was accomplished via the direct current potential drop (DCPD) method [20]. Standard 1T-CT specimens as described in ASTM E1820 were used with the sample machined such that cracking occurred along the weld centerline from the root of the weld, propagating toward the outside of the weld [23].

Samples were precracked in air in accordance with ASTM E1820 and then transferred to the BWR environment. At this point the sample was subjected to a series of cyclic sine wave loading steps at decreasing frequency and increasing load ratio R (P_{min}/P_{max}, where P=load) as a slow approach to constant loading. The final step prior to constant K loading was usually a trapezoidal load pattern with a 9000 s hold time. In this way the crack was preconditioned and sharpened to promote initiation of SCC crack growth. The preconditioning process usually lasted approximately 1700 h before constant loading was established. Once static loading was achieved sufficient time was allowed for a crack extension of the order of 1 mm to insure adequate accuracy, to insure that the previous plastic zone was

not an influence (100-350 m) and to insure an accurate crack length determination. The last step in each test consisted of a fracture toughness test. In this study we report on SCC crack growth rate (CGR) tests of as-welded, and at 673 K (400 °C) for 5000 h aged high- and low-ferrite welds.

2.2.5. Fracture Toughness Testing

Fracture toughness testing was performed using 1T-CT specimens machined so that the crack plane was coplanar with the weld centerline (Figure 1). The 1T-CT specimen was constructed and the fracture toughness tests were carried out in accordance with ASTM E1820 [23]. Pre-cracking for all test conditions was always performed to approximately the same a/W value of 0.58-0.64 as it was likely that the properties of a welds may change as a function of the location in the weld. Crack length was measured using the direct current potential drop (DCPD) method [20]. For material tested in air, load was applied by an Instron® 8500R load frame with temperature control provided by a 6.9 kW Thermocraft furnace. *In-situ* testing was performed in the SCC autoclave apparatus as described above. For all tests the extension rate was 0.02 mm/min for *in-situ* and 0.15 mm/min for tests in air with data taken continuously by the DAC system. High- and low-ferrite as-welded weld metals were tested at 298 K (25 °C), 561 K (288 °C), as well as *in-situ*. In addition material aged at 673 K (400 °C) for 5000 h was tested *in-situ*.

3. Results

3.1. Nanoindentation Hardness Results

Figure 2 shows a representative weld microstructure with a nanoindentation test matrix; δ-ferrite is the dark phase. The microstructure is typical of that in which the initial solidification phase is δ-ferrite which partially decomposes to austenite upon cooling; the so-called FA solidification mode [24]. The dendrite size can be approximated based on the spacing in between the δ-ferrite. The spacing correlates well with the SCC cracking morphology.

Figures 3 presents results of the nanoindentation measurements. An increase in indentation hardness (HIT) of δ-ferrite is clearly visible at each aging temperature. As the aging temperature increases, so does the hardening rate of δ-ferrite [about 7000 MPa after 40 000 h at 573 K (300 °C) compared to 9300 MPa after 10 000 h at 703 K (430 °C)]. Indentation hardness of austenite remains the same during aging, as expected. When comparing the different regions of the welds (root, middle, and crown), only small differences can be seen in the hardness values. In general the hardening rate is similar in each region. Yield and ultimate strengths [20] are presented together with the indentation hardness values. During ageing a small drop in yield strength and a small rise in ultimate tensile strength can be observed. The higher aging temperatures increase the ultimate strength more than aging at 573 K (300 °C) and during the first 1000 h the yield strength is also slightly increased.

Standard deviations are presented with black and grey lines for δ-ferrite and austenite, respectively. The deviations are higher for δ-ferrite than for austenite due to a much smaller fraction of δ-ferrite in the welds compared to that of austenite. For example, the thickness of the measured δ-ferrite areas may have been small, resulting in austenite below the δ-ferrite affecting the measured values. Also, the number of data points for δ-ferrite was much lower than for austenite.

3.2. DL-EPR Results

DL-EPR polarization curves are presented in Figure 4 and separated according to the aging temperature. The as-welded condition is shown in each of the three graphs for comparison purposes. No proper reactivation peak was observed for any other condition than the weld materials aged at 703 K (430 °C) for 5000 h and for 10 000 h (lower right graph in Figure 4). The reactivation scan peak current and activation scan peak current ratios (I_r/I_p) were 0.01 and 0.05, respectively. To be exact, a very small reactivation peak can be seen for the specimen aged at 673 K (400 °C) for 10 000 h as well but the I_r/I_p ratio is zero.

Figure 5 presents an overview of the DL-EPR specimens after testing. The as-welded (Fig. 5a) and at 573 K (300 °C) for 40 000 h aged (Fig. 5b) specimens did not show any sign of corrosion attack, whereas the specimens aged at 703 K (430 °C) for 5000 h (Fig. 5c), and 10 000 h (Fig. 5d) show a clear corrosion attack on the entire surface. The same can be seen in Figure 6 with higher magnification. The as-welded (Fig. 6a) and at 573 K (300 °C) for 40 000 h aged (Fig. 6b) specimens show a relatively smooth surface with austenite a little depressed when compared to δ-ferrite. The specimens aged at 703 K (430 °C) (Fig. 6c and d) show a rough surface with clearly visible corrosion on austenite. G-phase precipitation, confirmed by TEM observations [25] and previously observed in aged weld metals [14, 15], can be seen inside the δ-ferrite grains. It becomes more pronounced as the ageing time increases. The fact that no G-phase precipitation is observed in the specimen aged at 573 K (300 °C) suggests that hardening of δ-ferrite at that temperature is due to spinodal decomposition occurring in nanometer scale. Therefore, it does not have a great effect on the local chromium depletion and it does not locally reduce the corrosion resistance. No $M_{23}C_6$ precipitation at δ-ferrite-austenite phase boundaries was visible, and therefore no subsequent sensitization was observed. Figure 7 presents a back-scatter electron image of the G-phase precipitation especially along dislocation lines in the 703 K (430 °C) 10 000 h aged specimen, as also presented in reference [9].

3.3. Charpy-V Impact Toughness Results

Charpy-V impact toughness results are shown in Figure 8. The general trend in the Charpy-V impact toughness data is a decrease with aging time and temperature, as well as testing temperature. The decrease saturates rather quickly. The data is consistent with the reported literature results [26-28]. The actual data showed a considerable scatter since the specimens were taken from different locations of the weld (root, middle, and crown). Details can be found in reference [20]. The reason for the quick saturation of the impact toughness data was studied with fractography. At room temperature δ-ferrite is brittle and shows cleavage fracture mode, while austenite phase exhibits ductile shear fracture. The impact energy is dependent on the degree of brittleness of the δ-ferrite phase and saturates when 100 % of δ-ferrite shows cleavage fracture.

3.4. SCC Crack Growth Results

Figures 9-12 present the results of the SCC crack growth studies. Figure 9 shows a summary of the SCC crack growth rate showing “Disposition Curves” for sensitized Type 304 stainless steel and low-

carbon grades of austenitic stainless steels [29] in Figure 9a, as well as results for the weld metals aged at 673 K (400 °C) for 5000 h, and for as-welded materials. The disposition curves represent upper bounds of the data in the literature for the respective materials. Figure 9b shows the average SCC crack growth rates for the as-welded and at 673 K (400°C) for 5000 h aged high- and low-ferrite materials. On average, thermal aging of weld metal results in an approximate 2x increase in crack growth rate when compared to the similar as-welded material. Comparing the results, the data suggests that there is a larger impact on the higher ferrite material, indicating that the change in SCC resistance is influenced by the δ-ferrite region, as that is the main variable in the weld metal. The slightly lower SCC crack growth rate of high-ferrite material can be considered as normal variation since the difference in the ferrite content was small and may be affected, for example, by the orientation of the dendrites. The SCC crack growth testing times ranged from 2 to 8000 h, which must be counted as an additional aging time at 561 K (288 °C). However, the nanoindentation, DL-EPR, and Charpy-V impact test results suggest that the additional aging at 561 K (288 °C) may not have a significant effect, because of the subtle effect of aging at 573 K (300 °C) to the hardness of δ-ferrite, corrosion properties, and saturation of the impact toughness.

The fractography presented here focuses on the as-welded low-ferrite material because the fracture surface morphology was similar for all specimens. Figures 10-12 show the fracture surface morphology that was typical for all of the *in-situ* SCC specimens. In each figure the direction of crack propagation is from left to right and the loading direction is perpendicular to the fracture surface. Figure 10 (a) shows a low magnification SEM fractograph of the regions of interest: the fatigue pre-SCC region, the SCC region, the post-SCC fatigue region setting up for the fracture toughness portion, and the fracture toughness test region from initiation (stretch zone) to stable tearing. Figure 10 (b) shows SCC fracture surface exhibits mainly transgranular brittle behavior. The secondary cracks are related, for the most part, to the delta ferrite skeleton and the cracks are approximately 20 to 100 µm apart which is of the order of the dendrite spacing.

Figure 11 shows the fracture surface at the transition zone between the pre-fatigue and the SCC region with increasing magnification from (a) to (c). While the transition between the fatigue and SCC regions appears at low magnification to be abrupt (Figure 10a), as with the transition from SCC to fatigue (Figure 12a), the transition is more gradual when viewed at higher magnification. Fatigue regions are characterized by the presence of an oxide layer consisting of oxide particles precipitated from the aqueous solution. The SCC regions only have a thin oxide film formed on the surface. This is in spite of the fact that the SCC region and the fatigue regions experience the same environment at the same time in many cases. One may argue that a key difference is crack enclave mass transport (pumping) in fatigue which does not occur under static loading in SCC. However, this does not explain the lack of oxide precipitation on the SCC surface during a fatigue step after the SCC step. No chemistry and temperature transients were observed during the tests. The only rational explanation for this effect is that for some reason the solubility of cationic species with respect to oxide precipitation is exceeded in fatigue, but not under static loading in SCC. This requires a particular/unique combination of metal dissolution, oxygen concentration, and pH. Moreover, the favorable conditions have to occur immediately behind the crack tip.

Figure 12 shows the fracture surface at the interface between the SCC and post-SCC fatigue regions in more detail. Recall that the test sequence for all of the tests consisted of: (1) a region of cyclic loading with increasing R and decreasing frequency to establish a sharp crack tip, (2) a region of constant K loading where SCC occurs, followed by (3) another region of cyclic loading to establish proper

conditions for the (4) J-R fracture toughness test. Figure 12 (a) shows the SCC region as well as the beginning of the fatigue region prior to the J-R test. The boundary between the SCC and fatigue region is marked by the white line. Figure 12 (b) shows a higher magnification fractograph of the region outlined by the red box in Figure 12 (a) with regions of ferrite and austenite identified. The boundary between the SCC and fatigue regions provides a key insight into the crack propagation process. While the "macro" crack propagation direction is from left to right, the details of the crack propagation process are more complicated. The "FA" solidification process results in a largely austenitic structure with residual skeletal δ-ferrite. Crack propagation proceeds along the δ-ferrite-austenite boundary, followed by lateral extension into austenite. Figures 12 (c)-(e) further illustrate the crystallographic nature of SCC propagation in austenite. Figures 12 (c) and (d) show a higher magnification secondary electron SEM image of the delta ferrite region, whereas in Figure 12 (e) a backscatter electron SEM image of the area same is presented. Sites of small particles on the fracture surface can be observed in Figure 12 (d). Figure 12 (e) reveals the particle sites with better contrast together with localized corrosion on slip lines visible in the inter-dendritic transgranular SCC fracture surface in the austenitic phase. The particles are small MnS inclusions which reside at the δ-ferrite/austenite interface. They are dissolved in the water during testing. Otherwise the δ-ferrite-austenite phase boundaries are smooth since no $M_{23}C_6$ precipitation and subsequent sensitization takes place in the low-carbon AISI 316L weld metal. No sign of G-phase precipitation, which occurs inside the δ-ferrite, was visible on the phase boundary of the SCC fracture surface.

The crack path is along the δ-ferrite/austenite phase boundary and through the inter-dendritic austenite. The results suggest that SCC crack propagation occurs in two parallel processes; fast crack propagation along the δ-ferrite-austenite phase boundary and slower crack propagation through the inter-dendritic austenite. The slower rate in the austenite slows down the more rapid propagation along the δ-ferrite-austenite phase boundary. When the δ-ferrite regions are not fully interconnected, the crack propagation through the interface between the austenite and the δ-ferrite regions will retard the overall crack propagation rate.

3.5. Fracture Toughness Test Results

Figures 13 and 14 summarize the fracture toughness test results. Figure 13 (a) shows the data for 673 K (400 °C) aged weld metal, while Figure 13 (b) shows the data for the as-welded materials. Figure 14 shows representative J-R curves for the as-welded material. The general trend is that the weld metal tested at 298 K (25 °C) shows the highest toughness, followed by the 561 K (288 °C) air toughness, and the *in-situ* toughness being the lowest. The fracture toughness decrease at elevated temperature is in agreement with Chopra et al. [2]. Furthermore, the decrease in fracture toughness at elevated temperature is also consistent with the tensile properties at elevated temperature [20]. The environmental effect on fracture toughness is significant. In air testing, there is a small increase in toughness after 1000 h aging at 673 K (400 °C), but the fracture toughness becomes essentially independent of aging time beyond this. The nanoindentation and Charpy-V data indicate that spinodal decomposition takes place already at aging of 1000 h at 673 K (400 °C). However, the Charpy-V impact toughness increases with increasing temperature, since at high strain rate δ-ferrite is less brittle at higher temperatures.

Figure 15 (a)-(c) shows fractography for the air-tested low-ferrite weld metal. Comparing this with the fractography for the *in-situ* tested material in Figure 16, the differences are considerable. (1) The

fatigue region morphology in the air-tested material exhibits ductile-striation behavior, while in the *in-situ* case the fatigue morphology exhibits a more crystallographic brittle-striation morphology. (2) The transition between the fatigue and stretch zone region is very distinct for the air-tested material, while in the *in-situ* case the transition shows first a transgranular brittle zone less than 100 m wide before the ductile stretch zone. (3) The initial crack propagation region in the stretch zone consists of featureless shear in the air-tested case, whereas it is very crystallographic in the *in-situ* case. Moreover, there is no obvious relationship between the crack propagation mode and the microstructure in the air-tested material, while with the *in-situ* tested material there is more of a correlation between the microstructure and the crack propagation mode, albeit less obvious than the connection between the microstructure and SCC crack propagation. Figure 16 (c) shows the entire fatigue/brittle/stretch zone region obtained using the "SE2" imaging mode that is more sensitive to the surface morphology.

The *in-situ* fracture toughness test was conducted after approximately 2400 h exposure to high-temperature water containing 300 ppb dissolved oxygen. The fracture toughness test was conducted after a fatigue step to provide the same initial conditions. The parameters for the fatigue pre-cracking (air/561 K (288 °C): K=26 MPa m, R=0.1, 15 Hz; *in-situ*: K=22.4 MPa m, R=0.3, 1 Hz) were the same for each test. The values of a/W for each test (air/561 K (288 °C): a/W = 0.580; *in-situ*: a/W = 0.648) were close to each other which insured that the weld metal cracking occurred at approximately the same location for each sample. Additionally, the cyclic plastic zone sizes at the onset of each test were similar (air/561 K (288 °C): ~ 75 m, *in-situ*: ~ 75 m) [30]. For reference purposes, the monotonic plastic zone size for the values of K explored was in the range 100-350 m. In both cases the increment in a/W taken before the fracture toughness test step was large enough to insure that the crack tip was growing with a plastic zone free from the influence of the previous step.

Figure 17 illustrates the fracture surface characteristics typical in the stable tearing region of low-ferrite as-welded material tested in (a) air at 561 K (288 °C), and (b) *in-situ* at 561 K (288 °C). The differences in morphology between the air and *in-situ* conditions are subtle. The *in-situ* fracture path appears more planar. Additionally, in the air sample the ductile dimple morphology consists of a bimodal distribution of sizes. The smaller dimples are associated with the δ-ferrite phase while the larger dimples are associated with the austenite phase. The ductile dimple fracture morphology depends on the distribution of MnS inclusions in the weld metal. They are evident at the bottom of the dimples in Figure 17 (a), but they are not present in the *in-situ* sample due to dissolution in the high temperature water environment.

4. Discussion

There is a clear transition from fatigue crack growth morphology to a much more brittle behavior when SCC occurs (Figures 10-12). Referring to Figure 10, the SCC region exhibits a high degree of brittleness including multiple secondary cracking. The secondary cracking follows the δ-ferrite-austenite boundary. From Figure 12 (b) it appears that the crack propagation mode consists of parallel events; cracking along the δ-ferrite-austenite boundary in parallel with subsequent (and likely slower) propagation in the inter-dendritic austenite. Thus, the aging effects in Type 316L weld metal have to be related to the δ-ferrite-austenite phase boundary to explain the enhanced SCC crack growth rate after aging. The δ-ferrite-austenite phase boundaries are smooth since no $M_{23}C_6$ precipitation with

subsequent sensitization takes place in the low-carbon AISI 316L weld metal. Traces of small round MnS inclusions, which reside at the ferrite/austenite interface, were observed.

Referring to Figure 9 (b), thermal aging of weld metal at 673 K (400 °C) for 5000 h results on average in an approximate 2x increase in the crack growth rate over the unaged as-welded weld metal. During thermal ageing the major change in material properties is related to the hardening of the δ-ferrite region, while the hardness of austenite phase stays the same. This results in an increasing strength mismatch between the δ-ferrite region and the surrounding austenite phase. The softer austenite will deform and strain harden at the crack tip plastic zone markedly more than the harder and more brittle δ-ferrite region. The stronger δ-ferrite region directs and localizes the plastic deformation to the austenite resulting in SCC crack propagation along the phase boundary and subsequent lateral crack extension into the austenite phase. The reason for the enhanced SCC crack growth rate after thermal aging is expected to be related to the increasing strength mismatch between the δ-ferrite region and the austenite, rather than to any microstructural phenomenon directly.

While the bulk chemistry is constant throughout the test, as evidenced by a constant autoclave inlet and exit conductivity as well as a constant electrochemical potential, it is likely that the crack tip chemistry is different depending on the loading mode. This is evidenced by the presence of precipitated oxide on the fatigue fracture surfaces and the absence of precipitated oxide on the SCC fracture surfaces. The fact that two fatigue fracture surfaces surround the SCC fracture surface and the SCC fracture surface still does not show precipitated oxides, is further confirmation that the crack tip chemistry must have been different. The morphology suggests that oxide precipitation occurs immediately behind the crack tip. The only internally consistent explanation for this behavior is that the crack tip potential, which is controlled by the crack tip chemistry, is lower in the SCC region. Under fatigue conditions we expect that oxygenated water will be available due to the pumping action. Thus, we expect that this alone will cause the crack tip potential to be higher in fatigue. However, the lack of precipitated oxide on the SCC fracture surface, in spite of this surface being subjected to the pumping action of the post-SCC fatigue step, demonstrates that the presence of oxygen is not sufficient. This suggests that an additional supply of cations from dissolution is also necessary at sufficiently high concentration to cause the precipitation reaction to occur. The crack growth rate in fatigue was approximately an order of magnitude higher than in SCC. Additionally, the cyclic plastic zone size in fatigue is considerably smaller than the monotonic plastic zone size. Thus, the concentrated plasticity in fatigue enhanced the dissolution rate at the crack tip. In addition, the fractographic evidence suggests that the δ-ferrite plays less of a separate role in fatigue than in SCC.

As Figures 13-17 demonstrate, there is a clear effect of the environment on the (J-based) fracture toughness behavior. Moreover, referring to the J-Δa curves in Figure 14, once crack propagation has initiated, the value of dJ/da is reduced to essentially zero for the low-ferrite material and approaches zero for the high-ferrite material for *in-situ* exposure. Since the tearing modulus is proportional to dJ/da, it is anticipated that the environmental effect acts also in the bulk in addition to the local crack tip behavior. This is further reinforced by the amount of specimen lateral contraction [20]. Figures 15-17 focus on the crack initiation/blunting region. For air exposure the behavior is ductile tearing without obvious difference between the austenite and delta ferrite phases. However, the *in-situ* behavior suggests that there is a microstructural connection between the pre-fatigue region and the blunting region. The blunting region exhibits crystallographic, brittle-like behavior. There is microstructural continuity between the fatigue and brittle regions, highlighted in Figure 16. Slip steps are clearly visible on the fracture surface in the blunting region. Additionally, as with the SCC behavior, the pre-

fatigue region is decorated with a precipitated oxide while the crack propagation region does not show this. This is in spite of the fact that the as-cracked specimen remained in the autoclave for several hours at temperature after the completion of the fracture toughness test. At the same time, there is no obvious difference in the fractography in the stable crack propagation regions between the air and *in-situ* exposure.

The *in-situ* fracture toughness behavior, a reduction in initiation toughness and tearing resistance, implies that the cause has to be present throughout the weld metal. The initial brittle blunting region suggests that crack tip chemistry may be playing a role in enhancing the concentration of an aggressive species immediately ahead of the crack tip. The fact that the size of the brittle region is approximately the same as that of the cyclic plastic zone suggests that enhanced plasticity is also important. SCC cracking occurs along the δ-ferrite-austenite interface in parallel with inter-dendritic propagation in the austenite phase. In *in-situ* fracture toughness testing there is some correlation between the microstructure and the brittle inter-dendritic crack propagation, albeit much less obvious than the connection between the microstructure and SCC crack propagation.

A possible explanation that rationalizes the observed behavior is the potential effects of hydrogen, both diffusible and trapped, which may play a role in the degradation processes. The effect of hydrogen on material behavior has been studied extensively in materials, including stainless steels and to some extent welds, associated with other industries not relevant to the BWR environment. With respect to the effect of hydrogen on crack propagation there is general consensus that in austenitic stainless steel welds the effect of hydrogen is to induce fracture along the δ-ferrite-austenite interface [31, 32]. The abrupt change in the microstructure and mechanical properties, which results in significant strength/strain mismatch between austenite and δ-ferrite, promotes fracture at the interface. It is also likely that the BCC/FCC crystal structure mismatch promotes dislocation pile-ups that will influence the fracture behavior. Luppo et al. [33] have shown that the δ-ferrite-austenite interface acts as a strong hydrogen trap. The results from Somerday et al. [34] show a significant degradation (60-90 %) of both the initiation toughness and tearing modulus (dJ/da) by hydrogen in weld metals of 21Cr-6Ni-9Mn stainless steel. Their results show that hydrogen promotes micro-crack formation at the δ-ferrite-austenite interface.

While the above results involve conditions that are significantly different from the results reported here (either higher hydrogen concentrations, stainless steels different from Type 316L, room temperature, etc.) the common factor is that the effect of hydrogen is accompanied by a change in fracture morphology. The effect of hydrogen on toughness and tearing modulus of stainless steel weld metal reported by Somerday et al. [34] is similar as observed here in *in-situ* fracture toughness testing. For confirming the presence of hydrogen in the specimens, the hydrogen contents of as-welded specimens and after high-temperature water exposure were determined by hot extraction using a Leybold-Heraeus H2A 2002 hydrogen analyzer where the sample is heated up to 1373 K (1100°C) and the total amount of evolving hydrogen is analyzed by a thermal conductivity detector. Additionally, thermal desorption spectroscopy (TDS) was used in which hydrogen desorption in the temperature range of 298…973 K (25…700°C) is measured with a mass spectrometer (diffusible hydrogen). It was found that the hydrogen content of as-welded weld material obtained by hydrogen analyzer was 2…4 ppm, but only 0.6…0.9 ppm was obtained by TDS. Base metal hydrogen content was 3…5 ppm by both techniques. After the whole *in-situ* test procedure the hydrogen content of the weld metal obtained by the thermal analyzer was 2…6 ppm, but the base metal hydrogen content had decreased to 0.5…0.7 ppm. The values obtained by TDS were reduced to 0.1…0.2 ppm for both weld and base metals. During the long-

term high-temperature water exposure the diffusible hydrogen contents of both weld and base metals seem to decrease, but in the weld metal there are numerous deep trapping sites which may result even in slightly elevated total hydrogen content. Despite the initial transgranular brittle zone less than 100 m wide before the ductile stretch zone, the differences in morphology between the air and *in-situ* fracture toughness specimens were subtle. The fracture path appeared more planar and the amount of specimen lateral contraction was markedly smaller in the *in-situ* tested fracture toughness specimens as compared to the specimens tested in air. These differences may be related to the effects of diffusible and non-diffusible trapped hydrogen in the *in-situ* fracture toughness of the stainless steel weld metal.

5. Conclusions

The results of the research reported here can be summarized as follows:

δ-ferrite hardening was observed by nanoindentation. At 573 K (300 °C) it is likely caused by spinodal decomposion of δ-ferrite. At 673 K (400 °C) and above significant G-phase precipitation was observed in the δ-ferrite matrix and on dislocation lines.

Precipitation of $M_{23}C_6$ carbides was not observed on the δ-ferrite-austenite phase boundaries due to the low interstitial content of C in the weld metal.

The Charpy-V impact energy decreases and saturates quickly with increasing aging time and temperature. After saturation 100 % of δ-ferrite exhibits cleavage fracture. The saturation of impact toughness depends on the ferrite content, testing temperature, as well as aging temperature.

SCC crack growth rate for Type 316L weld metal is higher than that for wrought material. SCC crack growth rate for thermally aged weld metal at 673 K (400 °C) for 5000 h is increased by approximately a factor of two (2x) over that for the unaged as-welded condition.

SCC crack growth occurs along the δ-ferrite-austenite phase boundary. SCC crack propagation occurs by a parallel process consisting of a combination of cracking of the δ-ferrite-austenite phase boundary, followed by a slower inter-dendritic crack growth in the austenite phase.

In-situ fracture toughness in 561 K (288 °C) high-purity water environment containing 300 ppb dissolved oxygen is significantly reduced when compared to air tested values at the same temperature. The environmental effect on fracture toughness consists of both, a reduction in initiation toughness, and a reduction in tearing modulus.

Fracture surfaces of *in-situ* fracture toughness test specimens show a region of brittle transgranular fracture prior to crack blunting, not observed in the air tested specimens. The fracture path appeared more planar and the amount of specimen lateral contraction was markedly smaller in the *in-situ* tested fracture toughness specimens when compared to the specimens tested in air.

The results of this research suggest that the increase in SCC crack growth rate after thermal ageing is related to the increasing strength mismatch between the δ-ferrite region and the

austenite, rather than to any microstructural phenomenon directly. The reduction of fracture toughness in high-temperature water may be affected by the presence of hydrogen. It is likely that hydrogen is generated both at the crack tip, as well as on other specimen surfaces. Both diffusible and trapped hydrogen play a role.

Acknowledgements

This work was performed as a result of collaboration between the H. H. Uhlig Laboratory at MIT, the Tokyo Electric Power Company, and Aalto University, Finland. The authors greatly appreciate the generous funding provided by Tokyo Electric Power Company and the additional funding provided from the ENVIS project of Finnish SAFIR2014 program. Mrs. Olga Todoshchenko and Mrs. Ulla Ehrnsten are acknowledged for assistance in the hydrogen content measurements.

References

[1] G. Slama, P. Petrequin, and T. Mager: SMIRT Seminar #6, Assuring Structural Integrity of Steel Reactor Pressure Boundary Components, August 29-30, 1983, Monterey, CA.

[2] D.J. Gavenda, W.F. Michaud, T.M. Galvin, W.F. Burke, and O.K. Chopra: NUREG/CR-6428, Argonne National Laboratory, 1996.

[3] H.M. Chung, and T.R. Leax: Mater. Sci. Technol., 1990, Vol. 6, pp. 249-262.

[4] T. Yamada, S. Okano, and H. Kuwano: J. Nucl. Mater., 2006, Vol. 350, pp. 47-55.

[5] J.K. Sahu, U. Krupp, R.N. Ghosh, and H.J. Christ: Mater. Sci. Eng., 2009, Vol. A508, pp. 1-14.

[6] J.D. Mithieux, and R. Fourmentin: Duplex Stainless Steels, Ed. J. Charles, EDP Sciences, France, 2010, pp. 413-425.

[7] N. Meyer, M. Mantel, A. Gauthier, and C. Bourgin: Rev. Metall., 2011, Vol. 108, pp. 213-223.

[8] G.A. Young, J.D. Tucker, N. Lewis, E. Plesko, and P. Sander: Proc. of the 15th Conference on Environmental Degradation of Materials in Nuclear Power Systems – Water Reactors, TMS, 7-11 August, 2011, Colorado Springs, CO, USA, CD.

[9] T. Hamaoka, A. Nomoto, K. Nishida, K. Dohi, and N. Soneda: Phil. Mag., 2012, Vol. 34, pp. 4354-4375.

[10] T.J. Nichol, A. Datta, and G. Aggen: Metall. Trans., 1980, Vol. 11A, pp. 573-585.

[11] M.B. Cortie, and H. Pollak: Mater. Sci. Eng., 1995, Vol. A199, pp. 153-163.

[12] J.M. Vitek: Metall. Mater. Trans. A, 1987, Vol. 18A, pp. 154-156.

[13] J.M. Vitek, S.A. David, D.J. Alexander, J.R. Keiser, and R.K. Nanstad: Acta Metall. Mater., Vol. 39, pp. 503-516.

[14] K. Chandra, V. Kain, V. Bhutani, V.S. Raja, R. Tewari, G.K. Dey, and J.K. Chakravartty: Mater. Sci. Eng., 2012, Vol. A 534, pp. 163-175.

[15] K. Chandra, V. Kain, V.S. Raja, R. Tewari, and G.K. Dey: Corros. Sci., 2012, Vol. 54, pp. 278-290.

[16] H. Abe, and Y. Watanabe: Metall. Mater. Trans. A, 2008, Vol. 39A, pp. 1392-1398.

[17] J. Hillard: Spinodal Decomposition, In Phase Transformations, Materials Park, OH: ASM International, 1970, pp. 359-70.

[18] J. Zhou, J. Odqvit, M. Thuvander, S. Hertzman, and P. Hedström: Acta Mater., 2012, Vol. 60, pp. 5818-5827.

[19] D.J. Kotecki, and T.A. Siewart: Weld. J., 1992, Vol. 71, pp. 171-178.

[20] T. Lucas: The Effect of Thermal Aging and Boiling Water Reactor Environment on Type 316L Stainless Steel Welds, Doctoral Thesis, MIT, Cambridge, MA, 2011.

[21] W.C. Oliver, and G.M. Pharr: J. Mater. Res.**, 2004, Vol. 19, pp. 3-20.**

[22] International Standard ISO 12732:2006(E), "Corrosion of Metals and Alloys-Electrochemical Potentiokinetic Reactivation Measurement Using the Double Loop Method", First Edition, 2006.

[23] ASTM: Standard Method for Measurement of Fracture Toughness, ASTM E 1820 – 01, ASTM International, 2001.

[24] J. C. Lippold, and D. J. Kotecki: Welding Metallurgy and Weldability of Stainless Steels, John Wiley and Sons, New Jersey, 2005.

[25] M. Ivanchenko, U. Ehrnstén, A. Forsström, R. Ballinger, and H. Hänninen: *to be published in:* "The 14th International Conference on Material Issues in Design, Manufacture, and Operation of Nuclear Power Plants Equipment", June 6-10, 2016, St. Petersburg, Russia.

[26] P.H. Pumphrey, and K.N. Akhurst: Mater. Sci. Technol., 1990, Vol. 6, pp.211-220.

[27] J. Nayak, K.R. Udupa, K.R. Hebbar, and H.V.S. Nayak: Bulletin of Mater. Sci., 2004, Vol. 27, pp. 511-515.

[28] W. J. Mills: Int. Mater. Rev., 1997, Vol. 42, pp. 45-82.

[29] JSME S NA1-2002, "Code for Nuclear Power Generation Facilities", Rules on Fitness-for-Service for Nuclear Power Plants, The Japan Society of Mechanical Engineers, October, 2002.

[30] R. W. Hertzberg: Deformation and Fracture Mechanics of Engineering Materials, 2nd Edition, John Wiley & Sons, 1995.

[31] J. Brooks, and A. West: Metall. Trans. A, 1981, Vol. 12A, pp. 213-223.

[32] J. Brooks, A. West, and A. Thompson: Metall. Trans. A, 1983, Vol. 14A, pp. 75-84.

[33] M. Luppo, A. Hazarabedian, and J. Ovejero-Garcia: Corr. Sci., 1999, Vol. 41, pp. 87-103.

[34] B. Somerday, M. Dadfarnia, D. Balch, K. Nibur, C. Cadden, and P. Sofronis: Metall. Mater. Trans. A, 2009, Vol. 40A, pp. 2350-2362.

Table 1. Chemical compositions of the weld metals.

Specification	C	Mn	Si	S	P	Cr	Ni	Mo	Cu
Weld wire - Low ferrite (FN 10)	0.022	1.85	0.44	0.001	0.021	19.34	12.68	2.51	0.26
Weld wire - High ferrite (FN 14)	0.015	1.75	0.35	0.014	0.017	19.2	12.3	2.61	0.05

Table 2. Aging matrix for the experimental study program.

	As-welded	1000 h	5000 h	10 000 h	20 000 h	40 000 h
No aging	O	-	-	-	-	-
573 K (300 °C)	-	-	O	O	O	O
673 K (400 °C)	-	O	O	O	-	-
703 K (430 °C)	-	O	O	O	-	-

Figure captions:

Figure 1. Schematics showing: (a) Weld ring orientation in the pipe, (b) orientation of compact tension (CT) specimen construction relative to weld metal, heat affected zone (HAZ), and base metal. Reprinted with permission from Ref. 20.

Figure 2. Typical nanoindentation matrix with two good hits on ferrite (darker phase). The large indentation marking in the lower left corner of the image is a depth offset measurement.

Figure 3. Nanoindentation hardness values for high ferrite weld metal aged at 573 K (300 °C), 673 K (400 °C), and 703 K (430 °C). In addition, yield and ultimate tensile strengths are presented with dashed lines and values on the secondary axis.

Figure 4. Polarization curves for high ferrite weld metal aged at 573 K (300 °C), 673 K (400 °C), and 703 K (430 °C) for times ranging from 5000 h to 40 000 h, compared to the polarization curve of the as-welded condition.

Figure 5. SEM micrographs of DL-EPR specimens tested in solution 1M H_2SO_4 + 0.1 M KSCN. (a) As-welded, (b) 573 K (300 °C)/40 000 h, (c) 703 K (430 °C)/5000 h, (d) 703 K (430 °C)/10 000 h. Magnification of 3000 x.

Figure 6. SEM micrographs of DL-EPR specimens tested in solution 1M H_2SO_4 + 0.1M KSCN. (a) As-welded, (b) 573 K (300 °C)/40 000 h, (c) 703 K (430 °C)/5000 h, (d) 703 K (430 °C)/10 000 h. Magnification of 30 000 x.

Figure 7. Back-scatter electron image of G-phase precipitation in δ-ferrite aged at 703 K (430 °C) for 10 000 h.

Figure 8. Charpy-V impact toughness test results: (a) Tested at 298 K (25 °C), and (b) tested at 561 K (288 °C). Results for low and high δ-ferrite content specimens are presented. Adapted with permission from Ref. 20.

Figure 9. (a) Summary of SCC crack growth rate data in high-temperature BWR water environment for as-welded and at 673 K (400 °C) aged high- and low-ferrite weld materials, together with design lines for sensitized 304 stainless steel and low-carbon grades of austenitic stainless steels [27]. (b) Summary of the average crack growth rate for as-welded and at 673 K (400 °C) aged materials. Adapted with permission from Ref. 20.

Figure 10. SEM fractographs of low-ferrite as-welded material: (a) Overview of the test showing pre-fatigue, SCC, post-SCC fatigue, and fracture toughness regions. (b) The SCC crack propagation region with secondary cracks. Adapted with permission from Ref. 20.

Figure 11. SEM fractographs of low-ferrite as-welded material showing SCC crack morphology at the transition between pre-fatigue and SCC regions. (a) General view of the transition zone from pre-fatigue to SCC. (b) Transition from pre-fatigue to SCC. (c) Details of SCC propagation along ferrite/austenite boundary followed by lateral extension into austenite. Adapted with permission from Ref. 20.

Figure 12. SEM fractographs of SCC fracture tip in low-ferrite as-welded material showing cracking morphology and the propagation process. (a) SCC region and the beginning of the fatigue region prior to the J-R test. (b), (c) Crack propagation along δ-ferrite-austenite boundary, followed by lateral extension into austenite. (d) δ-ferrite surface with sites of small dissolved particles marked with red arrows. (e) Backscatter electron image revealing the particle sites on δ-ferrite surface and localized corrosion on slip lines in austenite. Adapted with permission from Ref. 20.

Figure 13. (a) Summary of J-based fracture toughness values as a function of aging time at 673 K (400 °C) for low- and high-ferrite weld materials. (b) Summary of J-based fracture toughness values for the as-welded condition of low- and high-ferrite weld materials. Adapted with permission from Ref. 20.

Figure 14. J-R curves for (a) low-ferrite, and (b) high-ferrite as-welded materials. *In-situ* fracture toughness is degraded compared to that in air at the same temperature. Reprinted with permission from Ref. 20.

Figure 15. SEM fractographs showing transition from fatigue crack to fracture toughness stretch zone in low-ferrite as-welded specimen tested at 561 K (288 °C) in air. Adapted with permission from Ref. 20.

Figure 16. (a) In-situ fracture toughness specimen stretch zone showing an initial brittle transition zone less than 100 μm wide not observed in air testing. (b) Transition from fatigue to fracture toughness loading in fractographic features is marked with black outlining. (c) Higher magnification of the brittle transition zone with clearly visible slip lines. Adapted with permission from Ref. 20.

Figure 17. Stable tearing region in low-ferrite as-welded fracture toughness specimens tested in (a) air at 561 K (288 °C), and (b) in-situ at 561 K (288 °C). Two distinct distributions of dimples are evident in both fracture surfaces. MnS inclusions are marked with red arrows. Adapted with permission from Ref. 20.

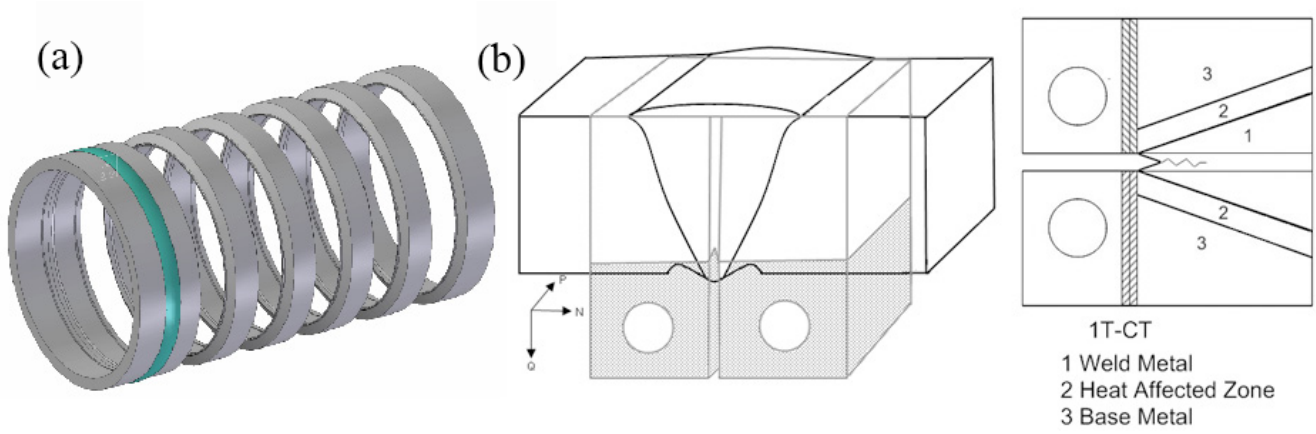

Figure 1. Schematics showing: (a) Weld ring orientation in the pipe, (b) orientation of compact tension (CT) specimen construction relative to weld metal, heat affected zone (HAZ), and base metal. [20] (reprinted)

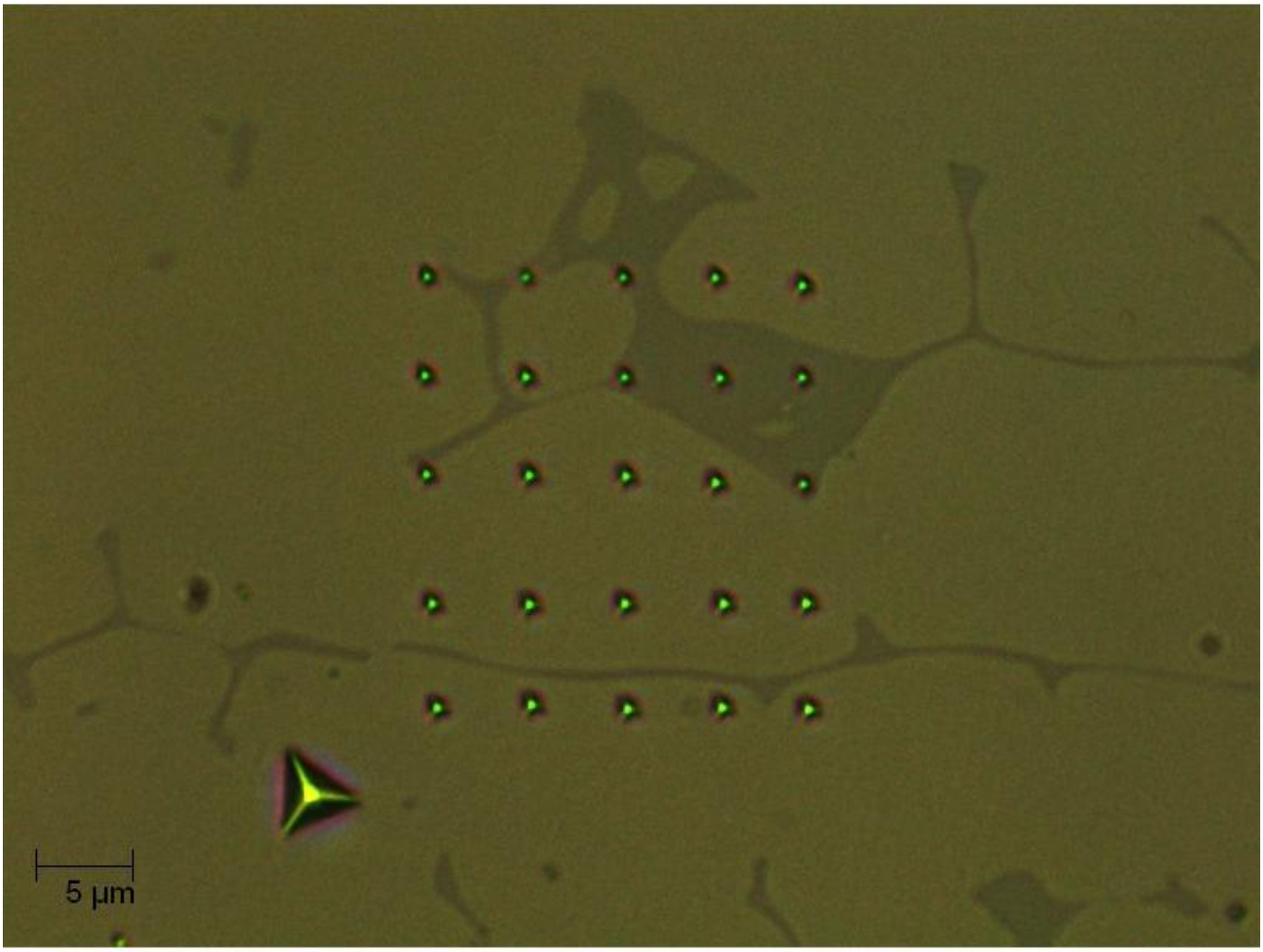

Figure 2. Typical nanoindentation matrix with two good hits on ferrite (darker phase). The large indentation marking in the lower left corner of the image is a depth offset measurement.

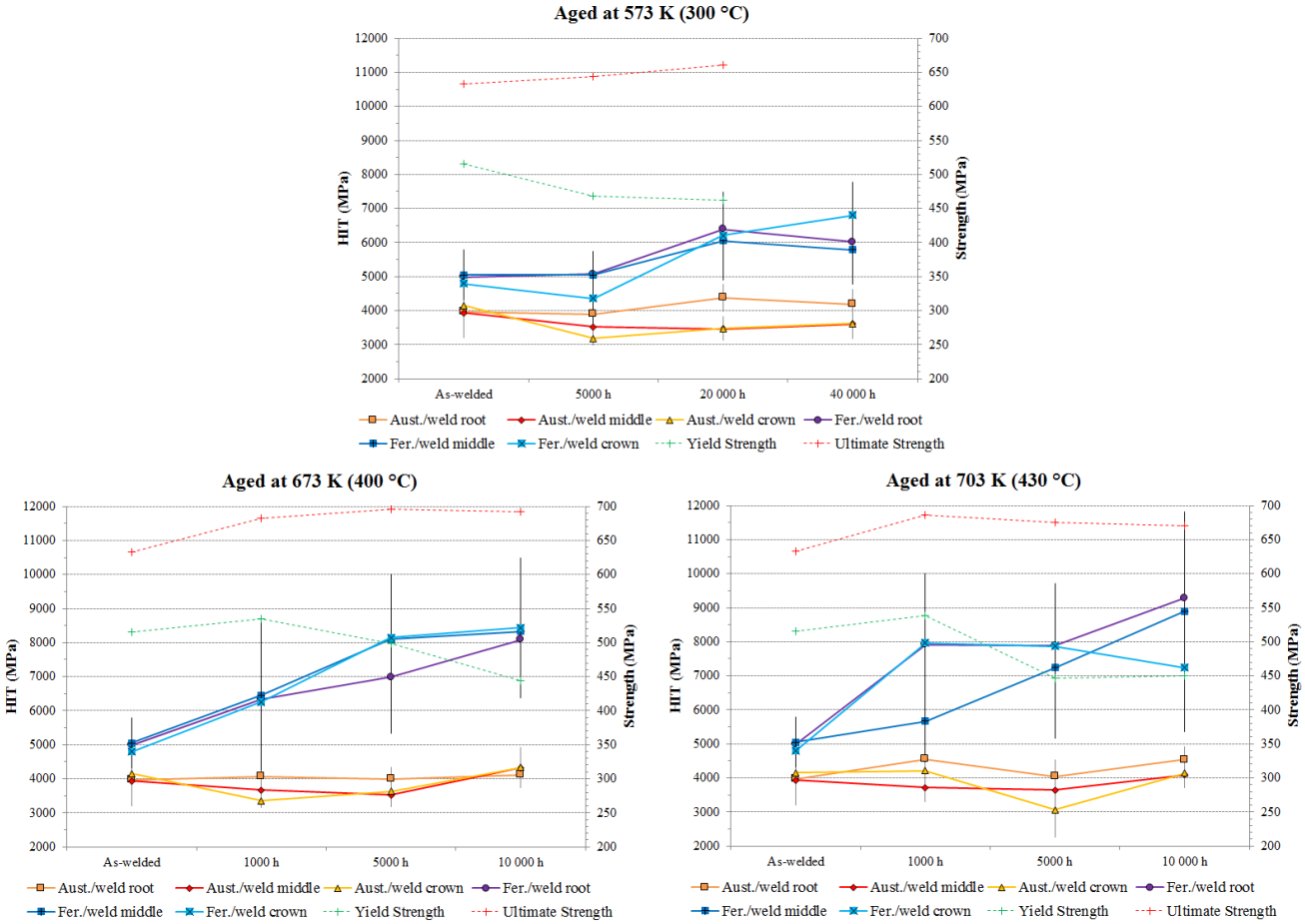

Figure 3. Nanoindentation hardness values for high ferrite weld metal aged at 573 K (300 °C), 673 K (400 °C), and 703 K (430 °C). In addition, yield and ultimate tensile strengths are presented with dashed lines and values on the secondary axis.

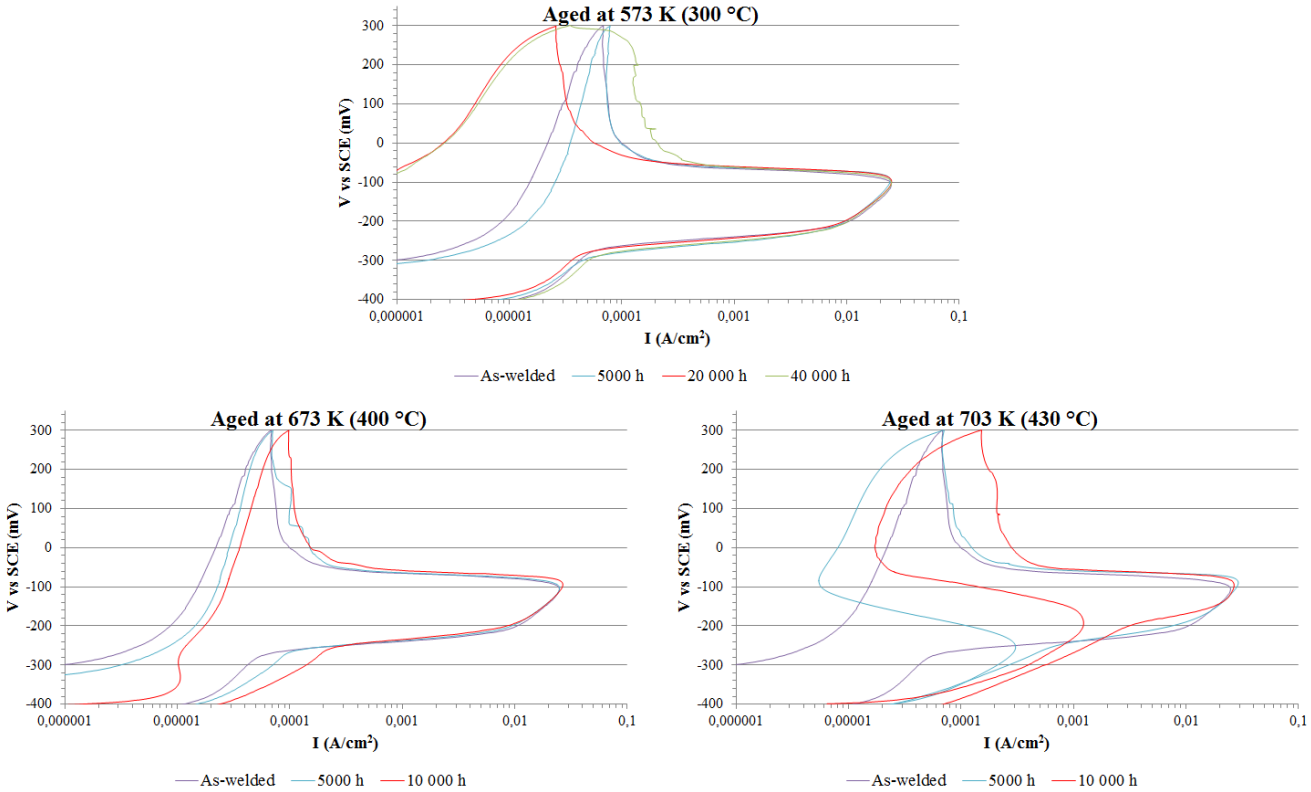

Figure 4. Polarization curves for high ferrite weld metal aged at 573 K (300 °C), 673 K (400 °C), and 703 K (430 °C) for times ranging from 5000 h to 40 000 h, compared to the polarization curve of the as-welded condition.

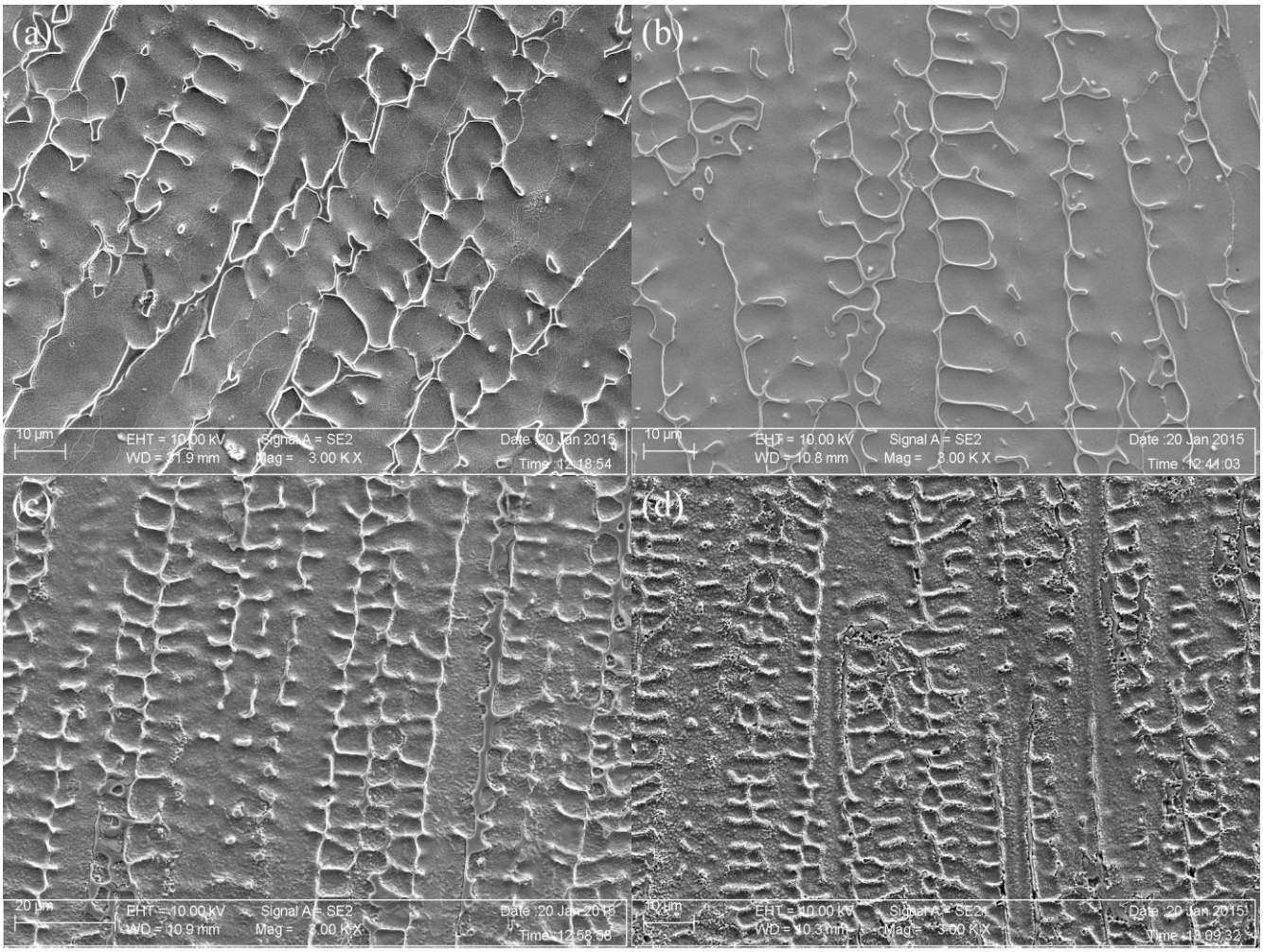

Figure 5. SEM micrographs of DL-EPR specimens tested in solution 1M H_2SO_4+ 0.1 M KSCN. (a) As-welded, (b) 573 K (300 °C)/40 000 h, (c) 703 K (430 °C) /5000 h, (d) 703 K (430 °C)/10 000 h. Magnification of 3000 x.

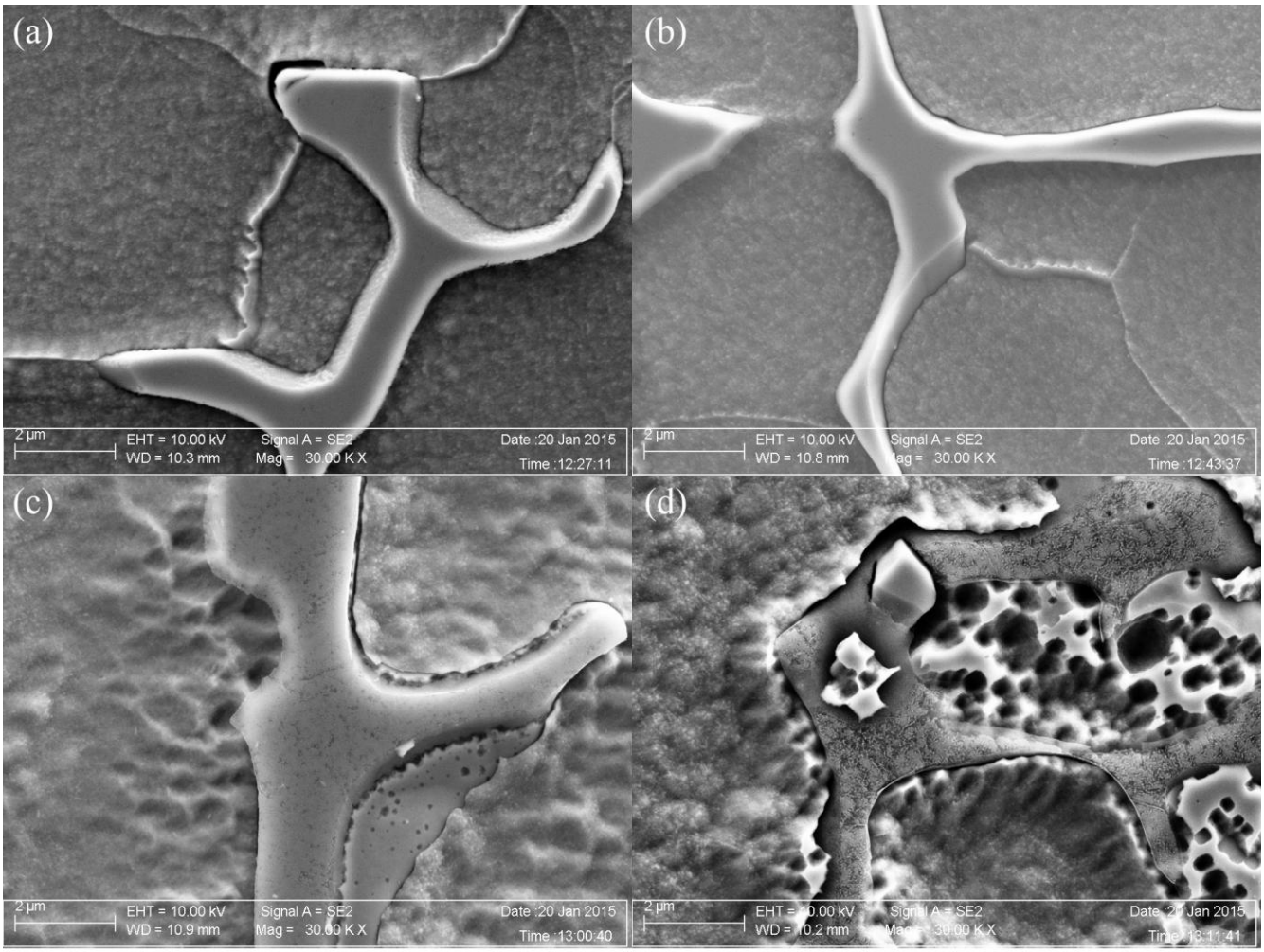

Figure 6. SEM micrographs of DL-EPR specimens tested in solution 1M H_2SO_4+ 0.1M KSCN. (a) As-welded, (b) 573 K (300 °C)/40 000 h, (c) 703 K (430 °C) /5000 h, (d) 703 K (430 °C)/10 000 h. Magnification of 30 000 x.

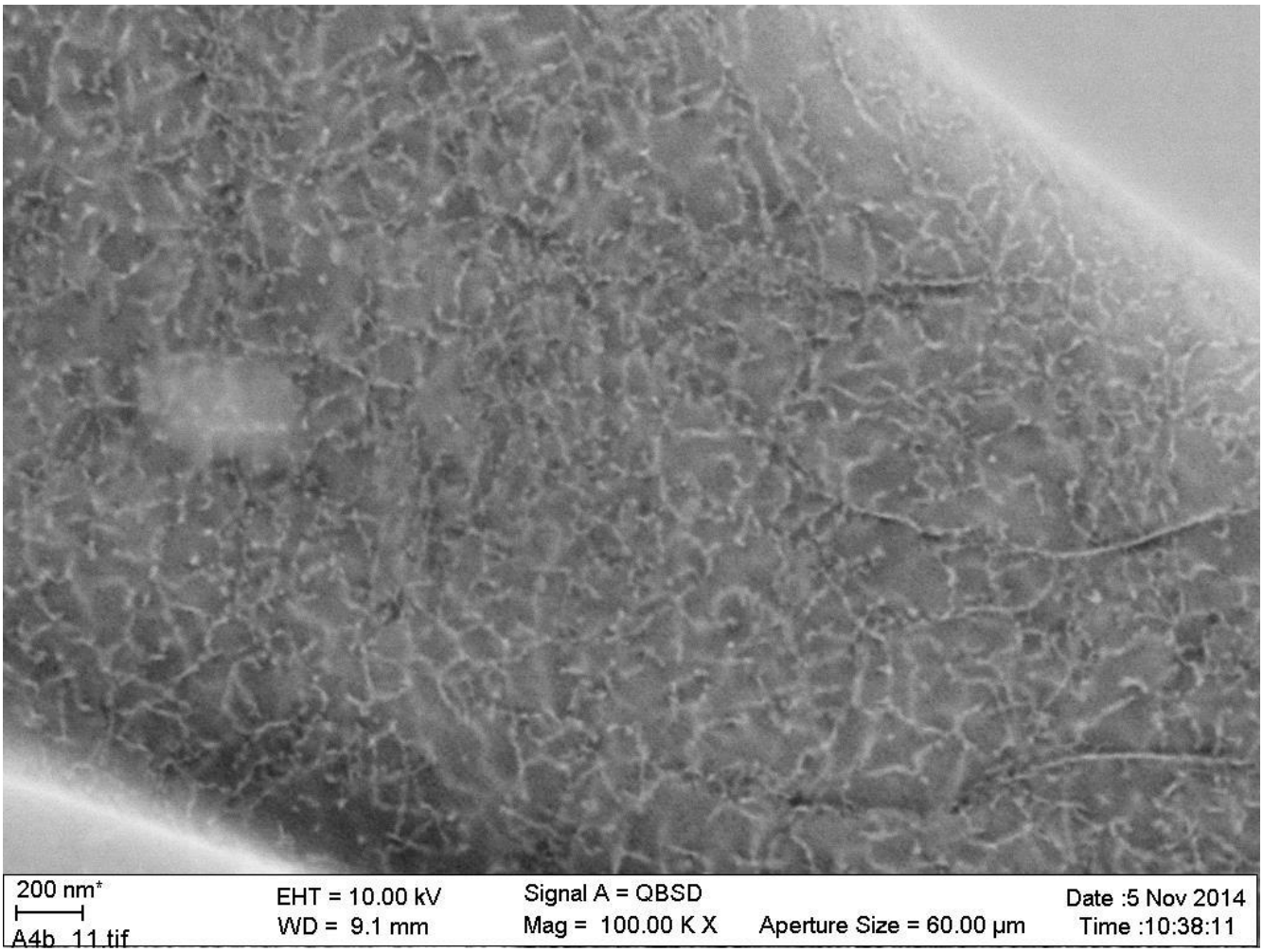

Figure 7. Back-scatter electron image of G-phase precipitation in δ-ferrite aged at 703 K (430 °C) for 10 000 h.

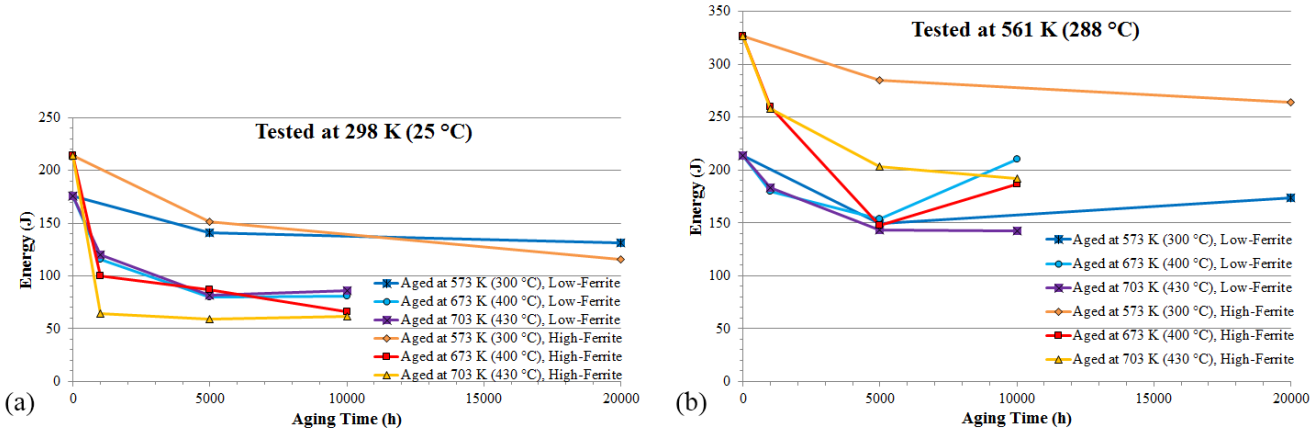

Figure 8. Charpy-V impact toughness test results: (a) Tested at 298 K (25 °C), and (b) tested at 561 K (288 °C). Results for low and high δ-ferrite content specimens are presented. [20] (adapted)

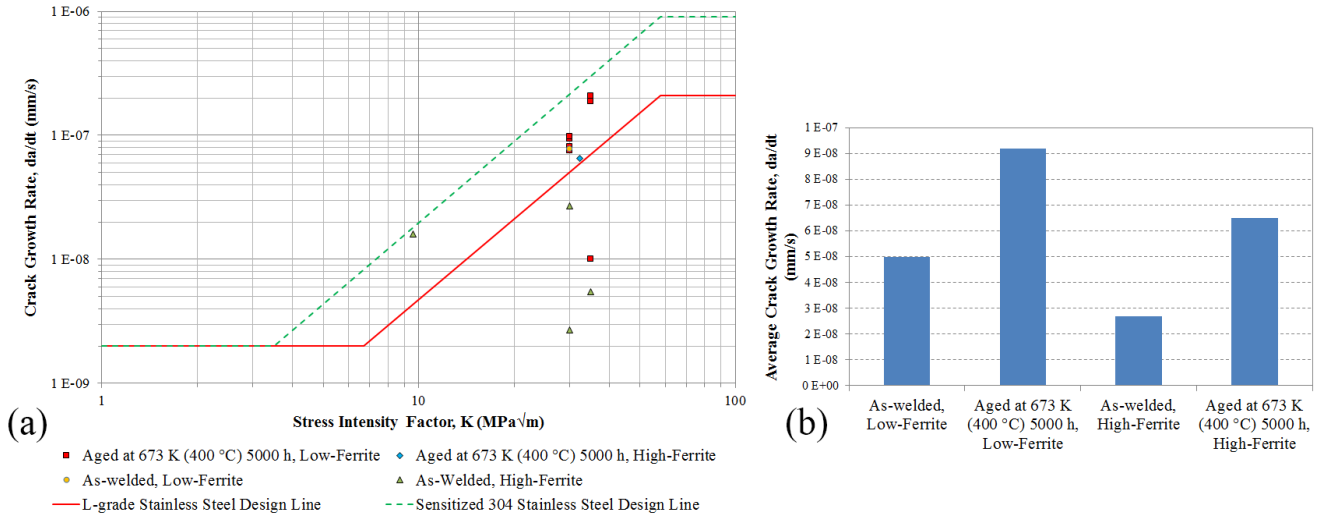

Figure 9. (a) Summary of SCC crack growth rate data in high-temperature BWR water environment for as-welded and at 673 K (400 °C) aged high- and low-ferrite weld materials, together with design lines for sensitized 304 stainless steel and low-carbon grades of austenitic stainless steels [29]. (b) Summary of the average crack growth rate for as-welded and at 673 K (400 °C) aged materials. [20] (adapted)

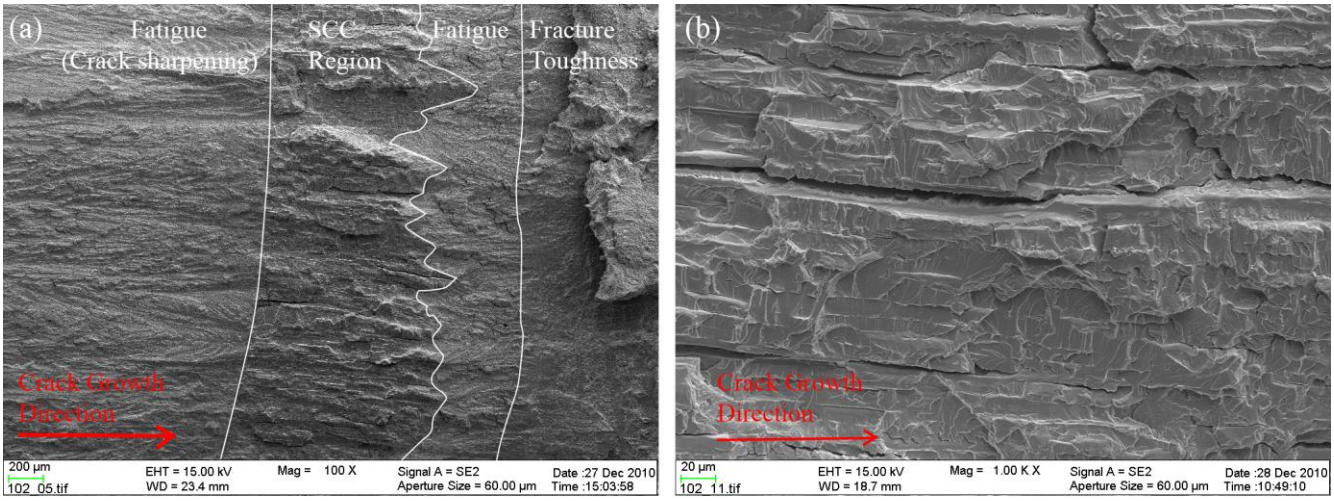

Figure 10. SEM fractographs of low-ferrite as-welded material: (a) Overview of the test showing pre-fatigue, SCC, post-SCC fatigue, and fracture toughness regions. (b) The SCC crack propagation region with secondary cracks. [20] (adapted)

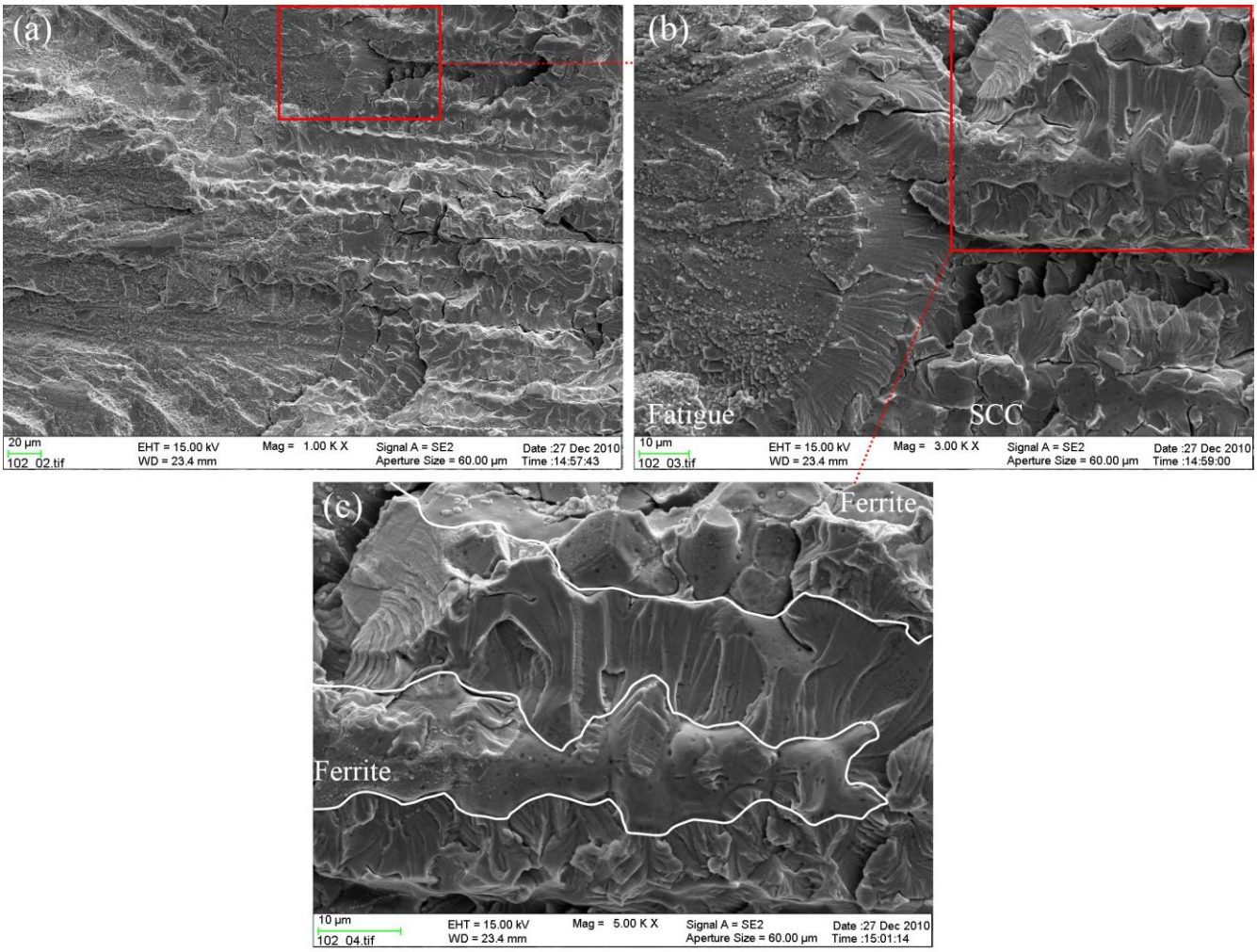

Figure 11. SEM fractographs of low-ferrite as-welded material showing SCC crack morphology at the transition between pre-fatigue and SCC regions. (a) General view of the transition zone from pre-fatigue to SCC. (b) Transition from pre-fatigue to SCC. (c) Details of SCC propagation along ferrite/austenite boundary followed by lateral extension into austenite. [20] (adapted)

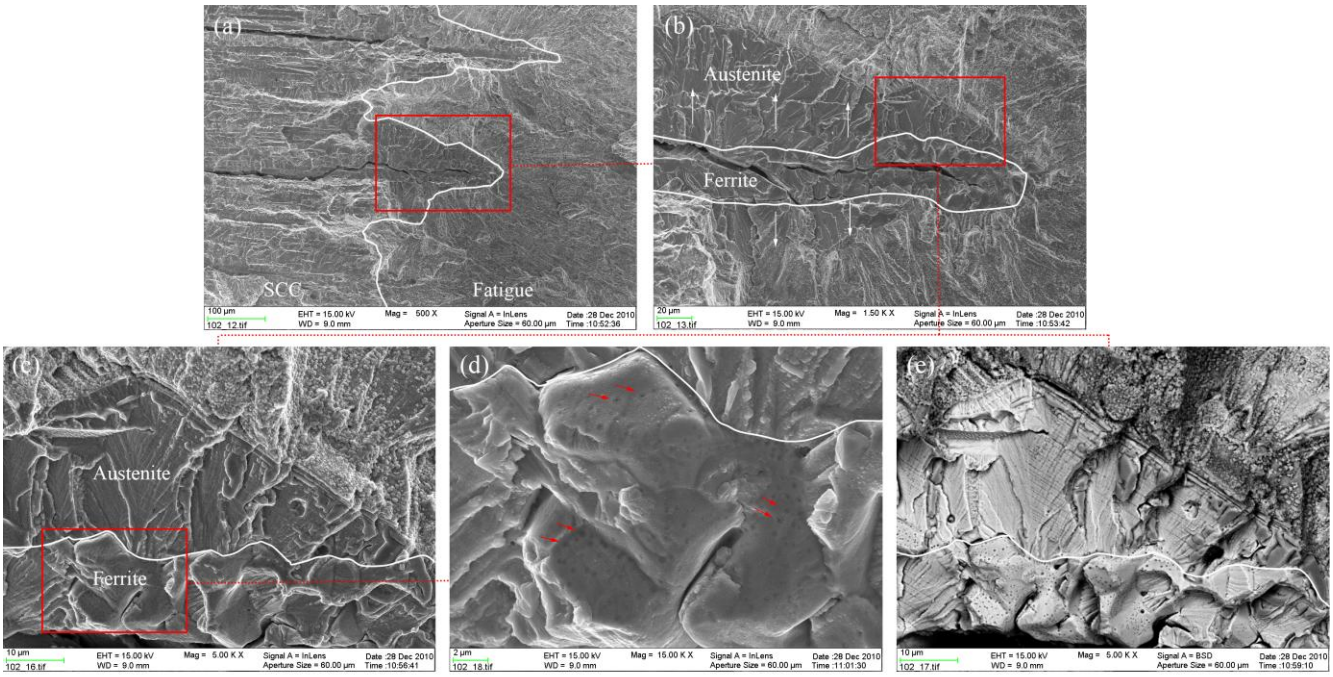

Figure 12. SEM fractographs of SCC fracture tip in low-ferrite as-welded material showing cracking morphology and the propagation process. (a) SCC region and the beginning of the fatigue region prior to the J-R test. (b), (c) Crack propagation along δ-ferrite-austenite boundary, followed by lateral extension into austenite. (d) δ-ferrite surface with sites of small dissolved particles marked with red arrows. (e) Backscatter electron image revealing the particle sites on δ-ferrite surface and localized corrosion on slip lines in austenite. [20] (adapted)

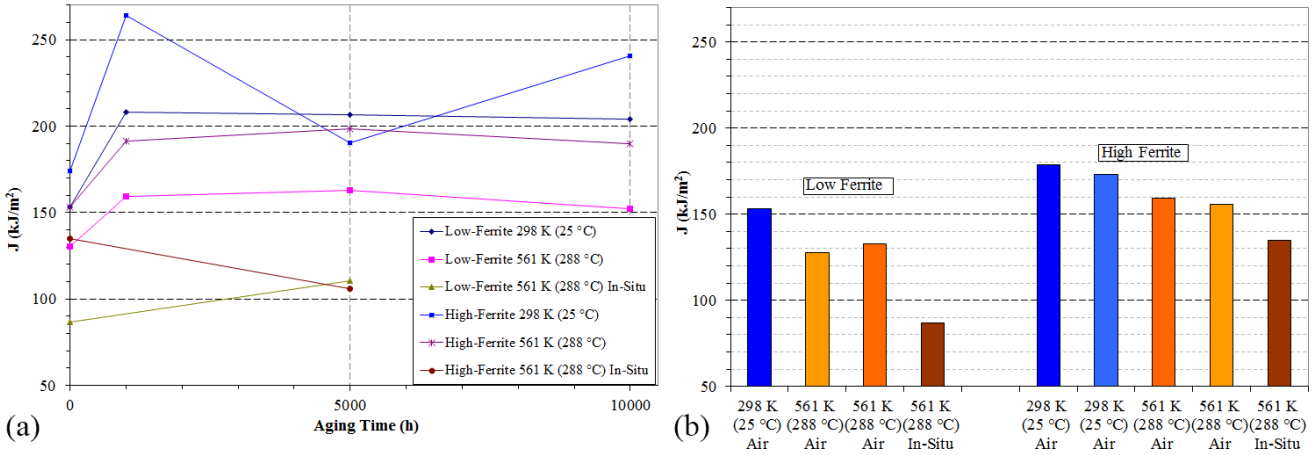

Figure 13. (a) Summary of J-based fracture toughness values as a function of aging time at 673 K (400 °C) for low- and high-ferrite weld materials . (b) Summary of J-based fracture toughness values for the as-welded condition of low- and high-ferrite weld materials. [20] (adapted)

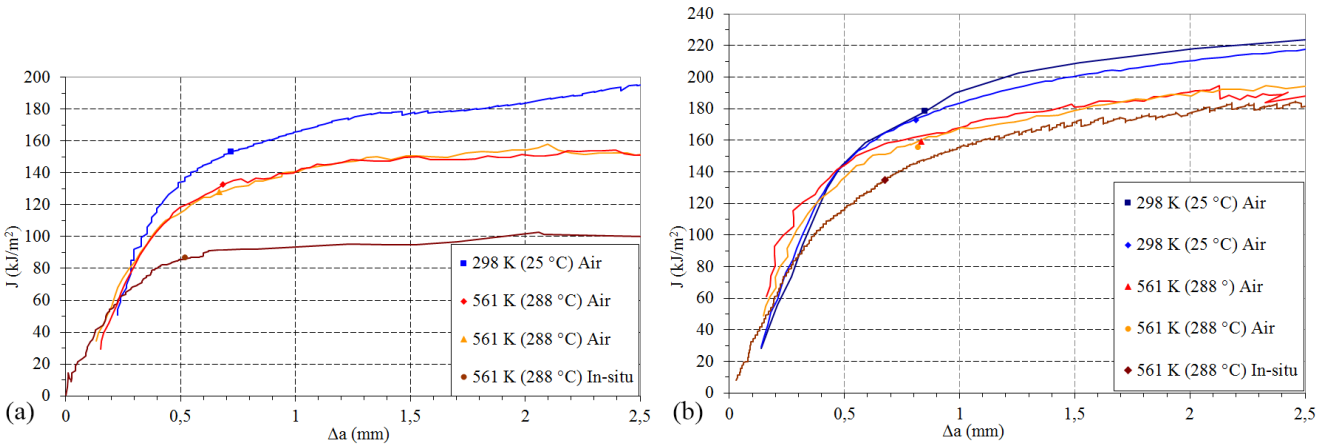

Figure 14. J-R curves for (a) low-ferrite, and (b) high-ferrite as-welded materials. *In-situ* fracture toughness is degraded compared to that in air at the same temperature. [20] (reprinted)

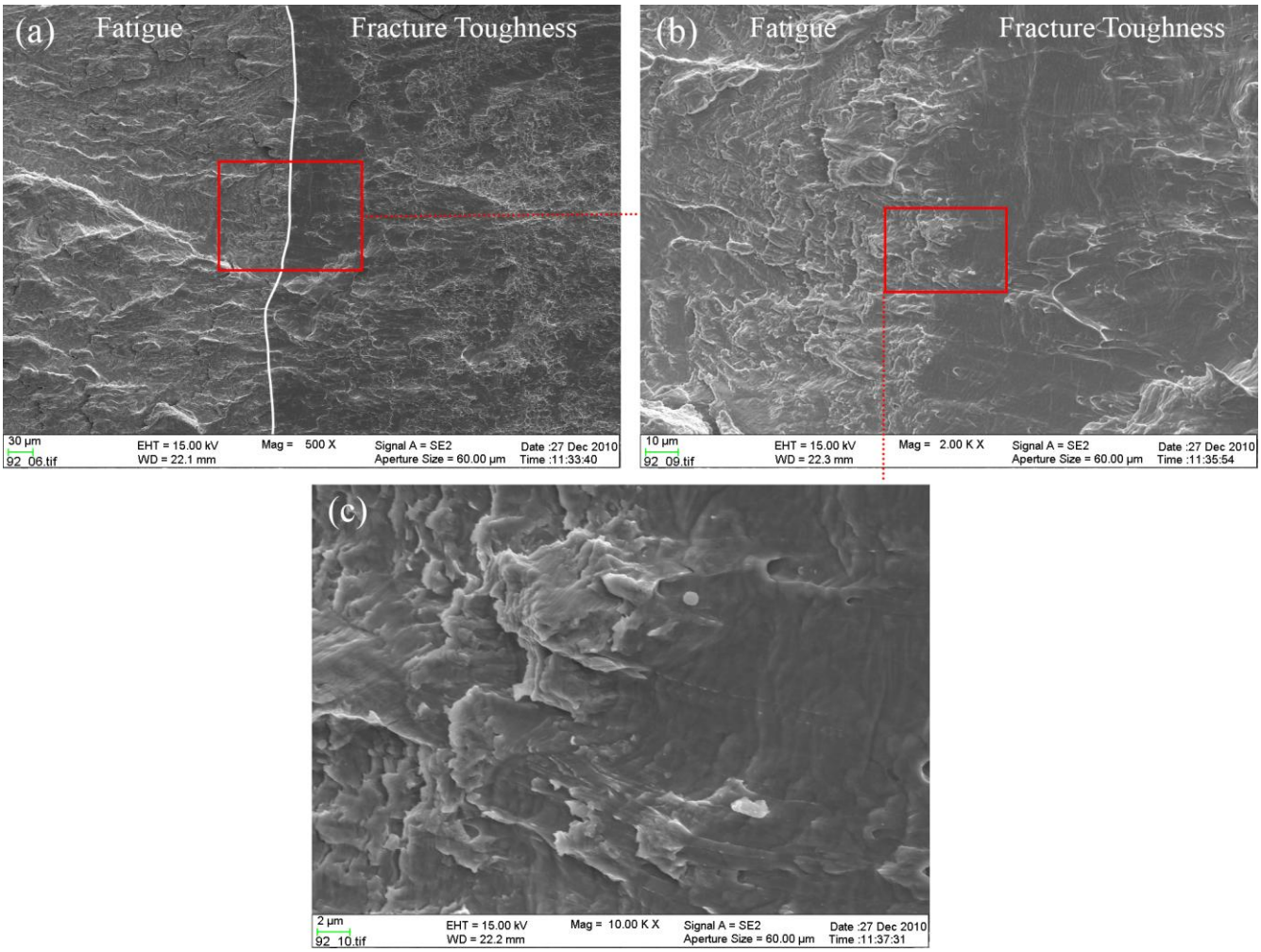

Figure 15. SEM fractographs showing transition from fatigue crack to fracture toughness stretch zone in low-ferrite as-welded specimen tested at 561 K (288 °C) in air. [20] (adapted)

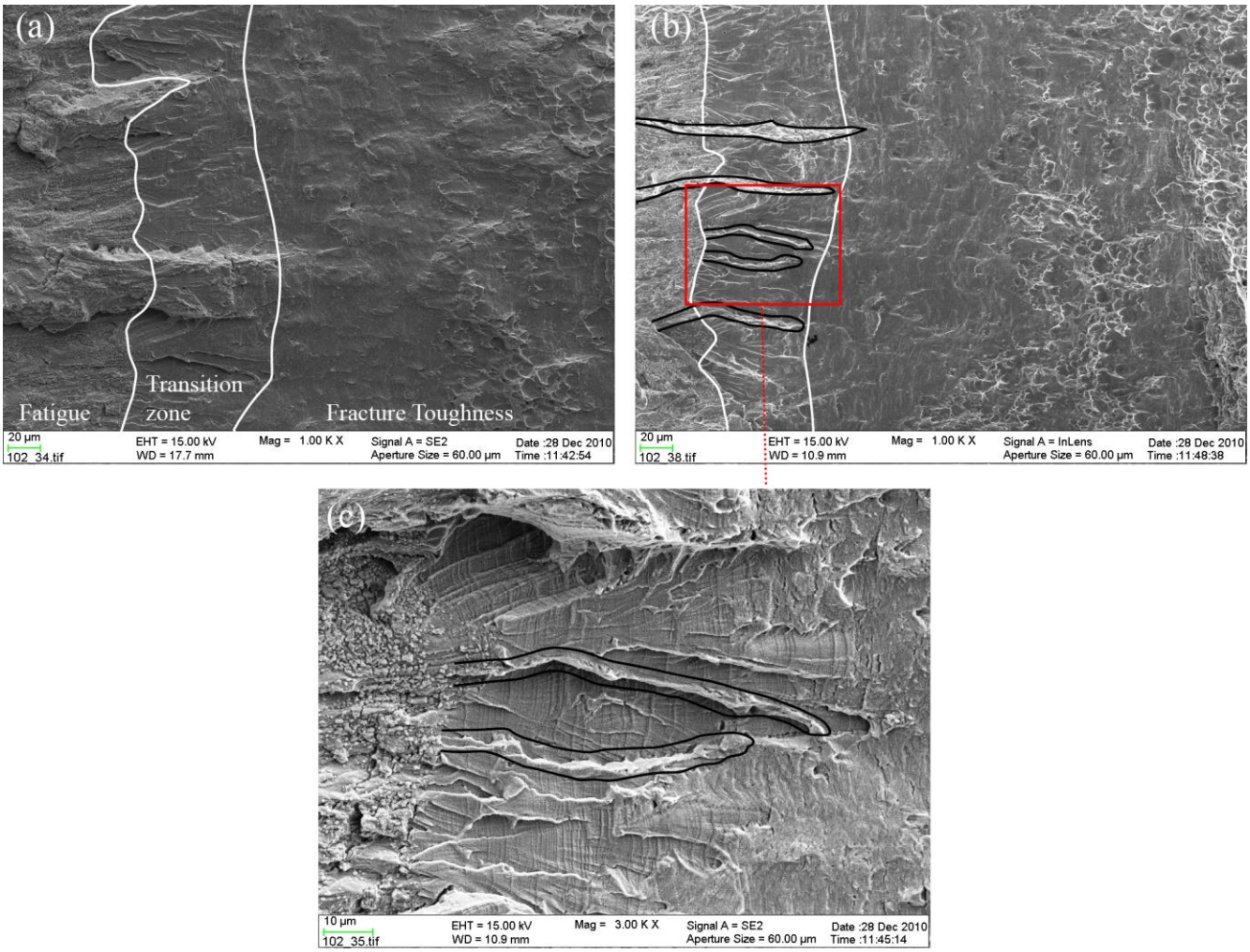

Figure 16. (a) *In-situ* fracture toughness specimen stretch zone showing an initial brittle transition zone less than 100 µm wide not observed in air testing. (b) Transition from fatigue to fracture toughness loading in fractographic features is marked with black outlining. (c) Higher magnification of the brittle transition zone with clearly visible slip lines. [20] (adapted)

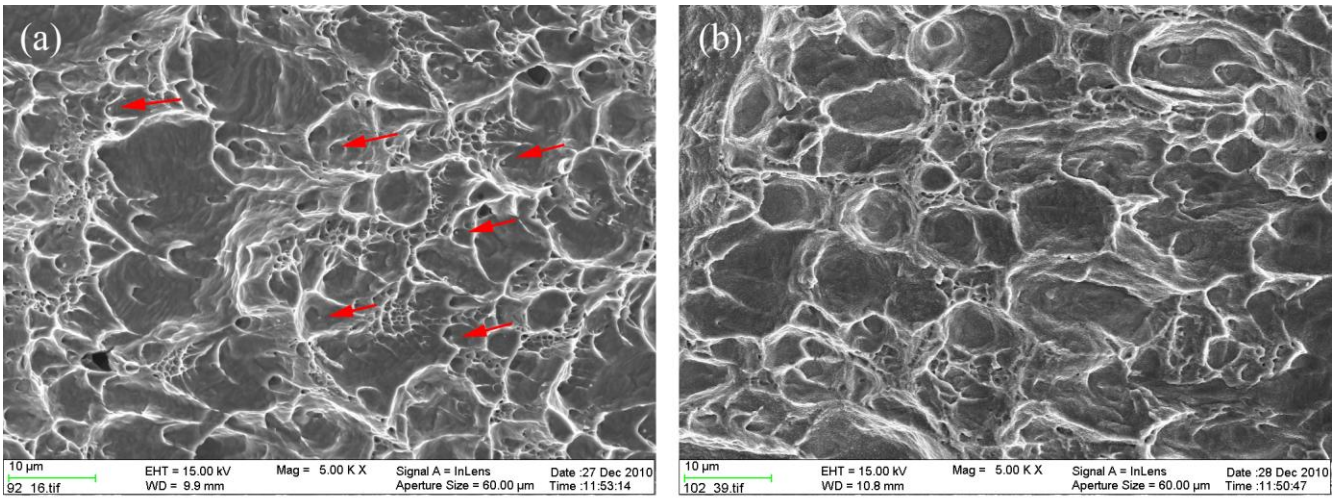

Figure 17. Stable tearing region in low-ferrite as-welded fracture toughness specimens tested in (a) air at 561 K (288 °C), and (b) *in-situ* at 561 K (288 °C). Two distinct distributions of dimples are evident in both fracture surfaces. MnS inclusions are marked with red arrows. [20] (adapted)